LLNL-JRNL-2015029

Turbulence simulations of Drift-Alfvén wave effects on edge-localized modes (ELMs) and divertor target heat flux width

N Li, X Xu

January 2026

Nuclear Fusion

This work performed under the auspices of the U.S. Department of Energy by Lawrence Livermore National Laboratory under Contract DE-AC52-07NA27344.

Turbulence simulations of Drift-Alfvén wave effects on edge-localized modes (ELMs) and divertor target heat flux width

X.X. He[1], T.Y. Xia[1*], Y.L. Li[1*], K.X. Fan[2], H.M. Qi[1], X.Q. Xu[3], Z.Y. Li[4], N.M. Li[3]
1 Institute of Plasma Physics, Chinese Academy of Sciences, Hefei 230031, China
2 School of Physics, Peking University, Beijing 100871, China
3 Lawrence Livermore National Laboratory, Livermore, CA 94550, USA
4 General Atomics, San Diego, CA 92186, USA

Abstract

A series of BOUT++ turbulence simulations are performed for two Pre-Fusion Power Operation (PFPO-1,2) phases of the ITER Research plan proclaimed in 2019. Linear simulation results show that PFPO-1 is unstable to Peeling-ballooning modes (PB), while the PFPO-2 is unstable to the coupling of PB and Drift-Alfvén wave (DAW) instabilities. The linear results are qualitatively consistent with the dispersion relation of DAW. To study the influence of the DAW on the edge-localized mode (ELM) crash, the PFPO-2 is adopted in this section. Different from the grassy ELM in [Li *et al 2022 Nucl. Fusion 62, 096030*], nonlinear simulations show that the ELM size of PFPO-2 is almost one-third of the grassy ELM, representing a distinct small ELM. However, simulations then show that if the PB instability is removed, the fluctuation amplitude drops by an order of magnitude and the ELM crash disappears, which is in accord with the theory in [Xu *et al 2010 Physical Review Letters, Vol. 105, 175005*] and the results in [Li *et al 2022 Nucl. Fusion 62, 096030*], confirming that the PB instability is a necessary condition for an ELM crash. Furthermore, removing the DAW drive also suppresses ELM crashes, implying that PB instability is necessary but insufficient for PFPO-2 ELM and that DAW could amplify PB-driven turbulence. In addition, by integrating results of both PFPO phases by BOUT++ turbulence analysis with heat flux width (λ_q) and electron thermal diffusivity (χ_e), these simulations establish a predictive framework for heat flux width and its dominant mechanisms, thereby providing a comprehensive scheme for the prediction of the heat flux width. Moreover, simulations indicate that DAW driving can increase the transport coefficient by enhancing the turbulent transport, leading to a broadened heat flux width once the transport coefficient exceeds its critical value.

Keywords: small ELM, turbulence, Drift-Alfvén wave, heat flux width

1. Introduction

The high confinement mode (H-mode), initially observed in 1982 on the ASDEX tokamak in Germany[1], is characterized by its superior plasma confinement properties. As a result, the H-mode is the planned operational regime for ITER and future fusion reactors[2]. However, this regime is always accompanied by periodic relaxations of the edge pressure gradient, known as edge-localized modes (ELMs)[3]. Although ELM events are beneficial in managing impurity density, their intense and sudden release of particle and heat fluxes could cause significant erosion of the divertor and impact tokamak operations[4-6]. A critical challenge that remains unresolved is how to withstand the substantial heat flux in future devices using the existing materials available for divertor targets. Heat flux control typically encompasses two main approaches: mitigating high transient heat fluxes through ELM suppression and reducing peak heat fluxes by expanding the scrape-off layer (SOL) power fall-off length, or called heat load width λ_q for high parameter future devices. Drift-Alfvén wave (DAW), as another major boundary macro-instability alongside ballooning mode and peeling mode, has been widely discussed: in 1978, the analytical theory of DAW was first proposed, suggesting that it can generate significant instability and affect plasma confinement under finite β conditions[7]; simulations using the fluid model BOUT++ and the gyro-fluid model GEMR on devices such as ASDEX-U, EAST, and C-Mod in I-mode have shown that DAW directly influences the formation and linear instability of the weakly coherent mode (WCM)[8-11]; in 2022, studies on EAST grassy ELMs indicated that DAW can delay the onset of ELMs while subsequently increasing the energy loss caused by ELM bursts[12]. The results of these studies collectively demonstrate that DAW can significantly affect turbulent transport. Therefore, it is essential to investigate the influence of DAW on ELMs. On the other hand, heat flux width has also been widely studied in recent years. In 2011, the Experimental (Eich) scaling, $\mathrm{\lambda_q} \sim 1/\mathrm{B_p}$, obtained based on multi-machine H-mode discharges, indicated that $\mathrm{\lambda_q}$ would be approximately five times smaller than the minimum limitation for ITER discharges[13-15]. Later in 2012, Goldston's Heuristic Drift Model, supported by experimental scaling, provided expressions of heat flux width at the divertor target based on the ion and electron drift[16]. Such narrow width will lead to unbearable thermal load, ultimately affecting the operation. Fortunately, studies including the qualitative and conceptual framework study presented by Myra in 2015, gyrokinetic simulations in 2017, magnetic fluid simulations under BOUT++ from 2019 and the latest SOLPS modeling with drifts all show that turbulent transport may enlarge SOL heat flux width[17-20]. Recent simulations under BOUT++ on multi-machine further demonstrate the competition between drift and turbulence in determining perpendicular cross-field transport by anomalous thermal diffusivity χ scan in SOL for ITER baseline scenario, CFETR baseline scenario and both Pre-Fusion Power Operation phases 1 and 2 (PFPO-1 and PFPO-2) scenarios proposed in the 2019 ITER Research Plan[21-26]. The critical value of the SOL thermal diffusivity χ_c has been put forward and discussed in Ref.19, 23. When the SOL thermal diffusivity $\chi > \chi_c$, radial transport transits from a drift-dominated to a fluctuation-dominated regime and the heat flux width would be enlarged.

BOUT++ is a 3D framework with a set of fluid equations for nonlinear finite-differencing simulations in edge plasma studies[27]. Within the BOUT++ framework, turbulence (six-fields two-fluid module) and transport simulation modules are developed separately, utilizing a similar set of Braginskii equations to capture the different physics in different temporal-scales[28-32]. Simulations conducted with turbulence and/or transport modules have yielded encouraging results on heat flux width and ELM analyses for devices such as EAST[33-41], C-Mod[22,42-44] and DIIID[45,46], as well as predictions for future machines like CFETR[21,47,48] and ITER[19,23]. Additionally, Using BOUT++ turbulence code, comparisons between simulation results and experimental data are performed for multiple current tokamaks' type-I ELMs, such as EAST[37,49], HL-2A[50], and DIIID[29,51], which yield a good agreement between numerical simulations and experiments. Therefore, BOUT++ can be reliably used to investigate the ELM dynamics and predict heat flux width λ_q.

The paper is organized as follows. Section 2 introduces setups and physical model of the BOUT++ elm-6f turbulence code used in this study. Section 3 presents the dispersion relation of the DAW and linear analyses for ITER PFPO scenarios. Additionally, the characteristics of ELM nonlinear dynamics for the PFPO-2 scenario, as well as the impact of PB mode and DAW on ELM and turbulence dynamics are also discussed in this section. Section 4 integrates turbulence simulations with prior scrape-off layer (SOL) coefficient scans from transport analyses to predict the divertor heat flux width for both PFPO-1 and PFPO-2 scenarios. Finally, the summary of simulations is given in section 5.

2. Simulation setups and physical model

2.1 Simulation equilibria

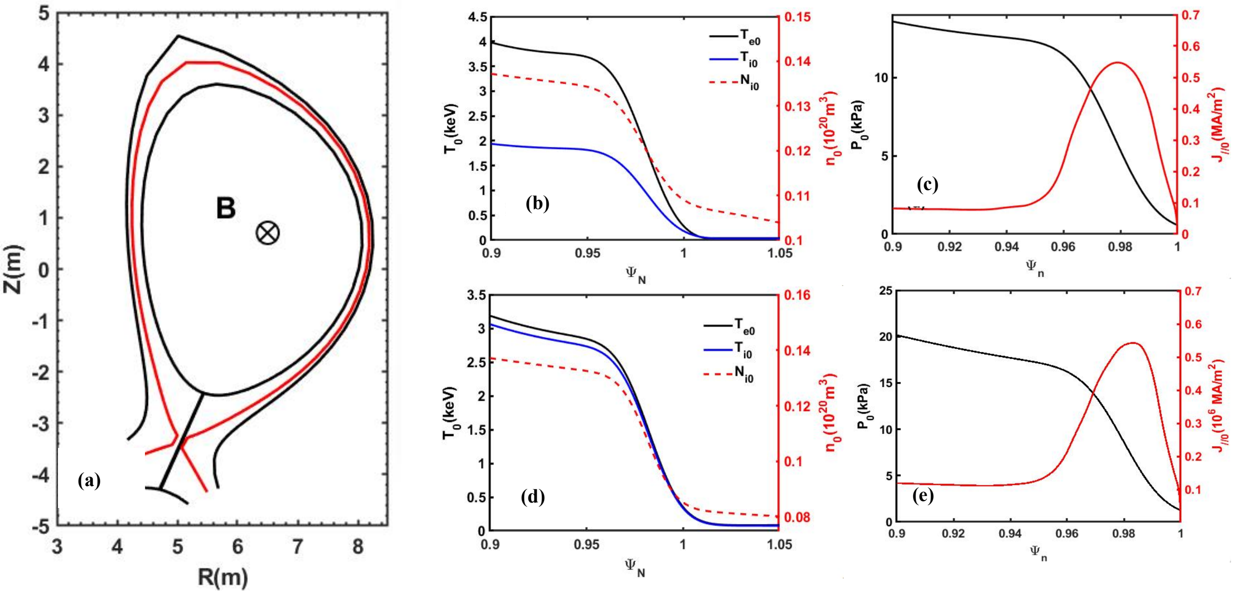

Figure 1. (a) Magnetic configuration and simulation domain. Plasma profiles of ITER 5 MA/1.77 T PFPO-1 scenario: (b) the electron temperature (black), ion temperature (blue) and ion density (red), profiles with $\mathbf{n_e} = \mathbf{n_i}$; (c) the pressure (black) and current density (red) profiles; Plasma profiles of ITER 7.5 MA/2.65 T PFPO-2 scenario: (d) the electron temperature (black), ion temperature (blue) and ion density (red), profiles with $\mathbf{n_e} = \mathbf{2n_i}$; (e) the pressure (black) and current density (red) profiles.

The simulation equilibria of the ITER 5MA PFPO-1 scenario and 7.5MA PFPO-2 scenario with lower plasma current, magnetic field and density consist of g-files and p-files generated using CORSICA[52,53]. Hydrogen (H) is the main ion species for the PFPO-1 scenario and helium (He) for the PFPO-2 scenario. The magnetic configuration of PFPO-2, similar to PFPO-1, is shown in figure 1(a). The simulation domain (between two black curves) is set as $\psi_N = 0.9 \sim 1.05$, where ψ_N is normalized poloidal magnetic flux. The red curve represents the position of the separatrix at $\psi_N = 1.0$. The resolution of both equilibria is 260×64 in the x, y

direction. The detailed initial profiles of ion density and temperature of PFPO scenarios are shown in figure 1(b) and figure 1(d). The temperature T_{e0} is similar to T_{i0} for PFPO-2 and the temperature T_{e0} is almost two times larger than T_{i0} for PFPO-1. The red dashed curve represents the ion density. The $n_{e0} = n_{i0}$ is applied for PFPO-1 while the $n_{e0} = 2n_{i0}$ is applied for PFPO-2 due to the different main ion species and no impurities considered. The radial profiles of initial pressure and current density of two scenarios are given in figure 1(c) and figure 1(e), respectively. The positions of the peak value of current and pressure gradient are at $\psi_N = 0.98$.

2.2 Physics model and equations of BOUT++ turbulence model

Simulations in this paper are carried out using the BOUT++ elm-6f turbulence module. The module incorporates physical effects such as drift waves, thermal conductivities, peeling-ballooning modes, diamagnetic drift, and ion acoustic waves, among others. Based on the full Braginskii equations and employing flute reduction, the elm-6f turbulence module consists of six evolving equations for density n_i, temperature T_e/T_i, ion parallel velocity $V_{\|i}$, vorticity ϖ and magnetic vector $A_\|$, which are written in the drift ordering. The equations are listed as follows[28]:

$$\frac{\partial N_i}{\partial t} = -\frac{1}{B_0} b \times \nabla_\perp \phi \cdot \nabla n_i - \frac{2n_i}{B_0} b \times \kappa \cdot \left(\nabla \phi + \frac{1}{Z_i e n_i} \nabla P_i\right) - n_i B_0 \nabla_\| \left(\frac{V_{\|i}}{B_0}\right) \tag{1}$$

$$\begin{aligned}\frac{\partial T_e}{\partial t} = &-\frac{1}{B_0} b \times \nabla_\perp \phi \cdot \nabla T_e - \frac{2}{3} T_e \left[\frac{2}{B_0} b \times \kappa \cdot \left(\nabla_\perp \phi - \frac{1}{e n_{e0}} \nabla P_e - \frac{5k_B}{2e} \nabla T_e\right) + \right.\\ &\left. B_0 \nabla_\| \left(\frac{V_{\|e}}{B_0}\right)\right] + 0.71 \frac{2T_e}{3e n_{e0}} B_0 \nabla_\| \left(\frac{J_\|}{B_0}\right) + \frac{2}{3n_{e0}k_B} \eta_\| J_\|^2 + \frac{2}{3n_{e0}k_B} \nabla_\| \left(k_{\|e} \nabla_\| T_e\right) + \\ &\frac{2}{3n_{e0}k_B} \nabla_\perp \left(k_{\perp e} \nabla_\perp T_e\right) - \left(\frac{2m_e}{M_i}\right) \frac{T_e - T_i}{\tau_e}\end{aligned} \tag{2}$$

$$\frac{\partial T_i}{\partial t} = -\frac{1}{B_0} b \times \nabla_\perp \phi \cdot \nabla T_i - \frac{2}{3} T_i \left[\frac{2}{B_0} b \times \kappa \cdot \left(\nabla_\perp \phi + \frac{1}{Z_i e n_{i0}} \nabla P_i + \frac{5k_B}{2Z_i e} \nabla T_i\right) + \right.$$

$$B_0\nabla_{\|}\left(\frac{V_{\|i}}{B_0}\right)\Big] + \frac{2}{3n_{i0}k_B}\nabla_{\perp}\left(k_{\perp i}\nabla_{\perp}T_i\right) + \frac{2}{3n_{i0}k_B}\nabla_{\|}\left(k_{\|i}\nabla_{\|}T_i\right) + \left(\frac{2Z_i m_e}{M_i}\right)\frac{T_e - T_i}{\tau_e} \tag{3}$$

$$\frac{\partial V_{\|i}}{\partial t} =-\frac{1}{B_0}b \times \nabla_{\perp}\phi \cdot \nabla V_{\|i} - \frac{b\cdot\nabla P}{n_{i0}M_i} \tag{4}$$

$$\frac{\partial \varpi}{\partial t} =-\frac{1}{B_0}b \times \nabla_{\perp}\phi \cdot \nabla\varpi + B_0^2\nabla_{\|}\left(\frac{J_{\|}}{B_0}\right) + 2b \times \kappa \cdot \nabla P + \mu_{i\|}\nabla_{\|,0}^2\varpi \tag{5}$$

$$\frac{\partial A_{\|}}{\partial t} =- \nabla_{\|}\phi + \frac{\eta}{\mu_0}\nabla_{\perp}^2 A_{\|} - \frac{\eta_H}{\mu_0}\nabla_{\perp}^4 A_{\|} + \frac{1}{en_{e0}}\nabla_{\|}P_e + 0.71\frac{k_B}{e}\nabla_{\|}T_e \tag{6}$$

In this model, vorticity ϖ, parallel current $J_{\|1}$ and parallel electron velocity $V_{\|e}$ are respectively defined as:

$$\varpi = n_{i0}\frac{m_i}{B_0}(\nabla_{\perp}^2\phi + \frac{1}{n_{i0}}\nabla_{\perp}\phi \cdot \nabla_{\perp}n_{i0} + \frac{1}{n_{i0}Z_i e}\nabla_{\perp}^2 p_{i1}) \tag{7}$$

$$J_{\|1} =-\frac{1}{\mu_0}\nabla_{\perp}^2 A_{\|} \tag{8}$$

$$V_{\|e} = \frac{n_i}{n_e}V_{\|i} - \frac{J_{\|1}}{en_e} \tag{9}$$

All variables in the equation set can be expressed as the sum of the equilibrium part of arbitrary field quantity F_0 and the perturbed component F_1, $F = F_0 + F_1$. In this module, the $E \times B$ drift velocity is calculated by potential $V_{E\times B} =-\frac{1}{B_0}b \times \nabla_{\perp}\phi$, Where ϕ is electrostatic potential. Here $b = b_0 + b_1$ is the unit vector of the total magnetic field, and $\kappa = b_0 \cdot \nabla b_0$ is the curvature parameter. The definition of pressure is $P = P_i + P_e$, in which the ion/electron pressure is $P_j = P_{j0} + P_{j1} = k_B n_j T_j$, $P_{j1} = n_{j0}T_{j0} + n_{j1}T_{j0} + n_{j1}T_{j1}$ for *j=i,e* species. The symbol $\kappa_{\|i}$, $\kappa_{\|e}$ is the ion/electron parallel effective thermal conductivity, which is the coupling of Spitzer-Harm thermal conductivity $\kappa_{\|i,e}^{SH}$ and the free-streaming expression $\kappa_{\|i,e}^{fse}$ as $\kappa_{\|i,e} = \frac{\kappa_{\|i,e}^{SH}\kappa_{\|i,e}^{fse}}{\kappa_{\|i,e}^{SH}+\kappa_{\|i,e}^{fse}}$. The expressions of Spitzer-Harm thermal conductivities are $\kappa_{\|i}^{SH} = 3.9n_i\upsilon_{th,i}^2/\nu_i$ and $\kappa_{\|e}^{SH} = 3.2n_e\upsilon_{th,e}^2/\nu_e$, where $\upsilon_{th,i,e}$ is the thermal velocity and $\nu_{i,e}$ is the collision rate. The expression of free-streaming is $\kappa_{\|i,e}^{fse} = n_{i,e}\upsilon_{th,i,e}qR_0$, where q is the local safety factor. The radial electrical field in the simulation is calculated using the formula $E_r = (1/$

$Z_i e n_i)\nabla_\perp P_i$, which considers the flow balance law without flow. η is defined as the parallel Spitzer resistivity, $\eta_s = 0.51 \times 1.03 \times 10^{-4} Z_i \ln\Lambda\, T^{-3/2}\ \Omega\mathrm{m}^{-1}$, where Z_i is ion charge number and $\ln\Lambda$ is coulomb logarithm. Hyper resistivity η_H, also known as electron viscosity, is essential for nonlinear simulations to limit the radial spreading of ELMs by facilitating magnetic reconnection. The neutral and impurity particles are neglected. In the simulations, sheath boundary conditions are imposed on the divertor targets. Neumann boundary condition is applied at the inner radial boundary, while Dirichlet boundary condition is for the outer radial boundary. For the core region, a twist-shift periodic boundary condition is set in the y direction and periodic boundary condition is used in the toroidal direction.

3. Impact of DAW on the ELMs

3.1 Dispersion relation of DAW

The DAW, driven by the electron pressure gradient, is an important electromagnetic instability of pedestal plasma. The dispersion relation of the DAW can be derived from the following four-field model, which excludes kinetic effects. The four-field equation set [54,55] is:

$$\frac{m_i n_{i0}}{B_0^2}\frac{\partial}{\partial t}(\nabla_\perp^2 \phi) - \nabla_\parallel J_\parallel = 0 \tag{10}$$

$$\frac{\partial n}{\partial t} + \frac{b_0 \times \nabla\phi}{B_0} \cdot \nabla n_0 - \frac{\nabla_\parallel J_\parallel}{e} = 0 \tag{11}$$

$$\frac{\partial T_e}{\partial t} + \frac{b_0 \times \nabla\phi}{B_0} \cdot \nabla T_{e0} - \frac{2}{3}\frac{T_{e0}}{e n_0}\nabla_\parallel J_\parallel = 0 \tag{12}$$

$$\frac{\partial A_\parallel}{\partial t} + \nabla_\parallel \phi - \frac{1}{e n_0}\nabla_\parallel P_e + 0.51\frac{m_e \nu_e}{e^2 n_0} J_\parallel = 0 \tag{13}$$

Since the ratio $L_{Te}/L_{ne} \sim 1$ in our PFPO scenarios, the ratio of the thermal force term to the parallel gradient of the electron pressure term is 1/3, which is at the similar order of magnitude to the inverse aspect ratio ε. Consequently, the temperature gradient in thermal force term is neglected in our model, and we primarily focus on the influence of the parallel gradient of the electron pressure term. In the equation (13), $\mathrm{J}_{\parallel}=-\frac{1}{\mu_0}\nabla_{\perp}^2\mathrm{A}_{\parallel}$ and the electron coulomb collision expression is $\nu_\mathrm{e}=\frac{4\pi\mathrm{n}\mathrm{Z}_\mathrm{i}\mathrm{e}^4\ln\Lambda}{(4\pi\epsilon_0)^2\mathrm{m}_\mathrm{e}^2\upsilon_{\mathrm{T}_\mathrm{e}}^3}$. Moreover, the quasi-neutrality assumption is retained in this model. Assuming the perturbation has the expression as $\{\tilde{\mathrm{n}},\tilde{\phi},\tilde{\mathrm{A}}_{\parallel}\}\sim\exp(-\mathrm{i}\omega\mathrm{t}+\mathrm{i}\boldsymbol{\kappa}\cdot\mathbf{r})$, and the reasonable assumption $k_\perp^2\rho_s^2\ll 1$ $(\rho_\mathrm{s}=\frac{c_s}{\omega_{ci}})$, we get the dispersion relation normalized by ν_e for the DAW:

$$(\widehat{\omega}^2-\widehat{k}_{\parallel}^2)(\widehat{\omega}-\widehat{\omega}_*)+0.51i(k_\perp^2d_e^2)\cdot\widehat{\omega}^2=0,\quad \widehat{\omega}_*=-\frac{k_\perp T_e}{eB\nu_\mathrm{e}}\frac{1}{\mathrm{L}_{\mathrm{pe}}} \tag{14}$$

Thereinto, $d_e^2=\frac{m_e}{e^2n_e\mu_0}$ is used to simplifiy the expression and the $\mathrm{L}_{\mathrm{pe}}=-\mathrm{P}_\mathrm{e}/\nabla\mathrm{P}_\mathrm{e}$ is the electron pressure characteristic length. For a certain equilibrium, the $\widehat{\omega}_*$ depends on L_{pe}. Therefore, the dispersion relation can be regarded as the function of the growth rate with the electron pressure characteristic length.

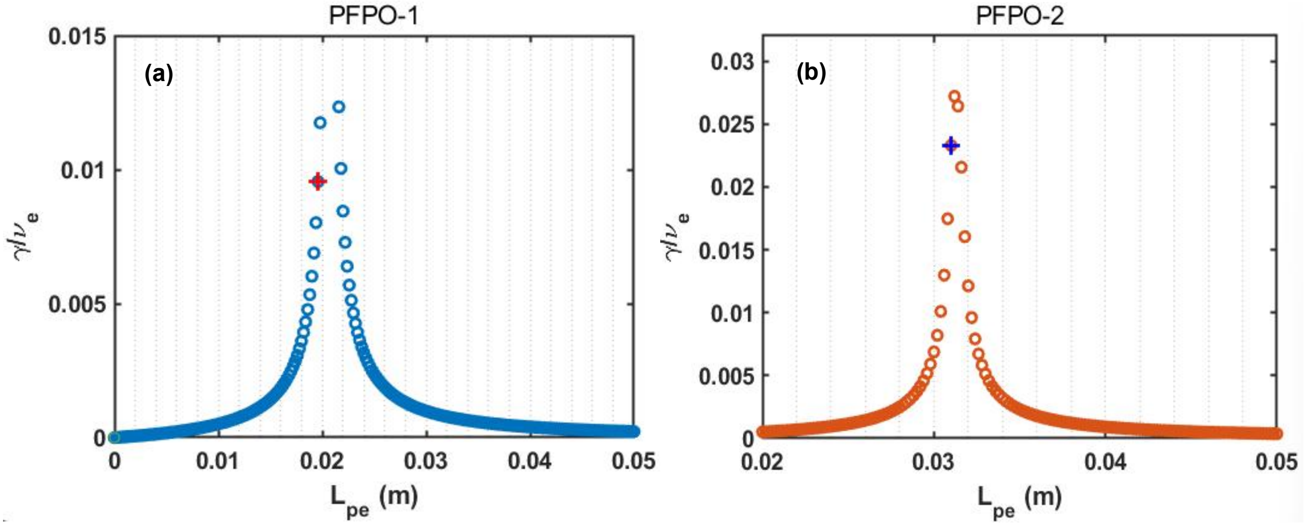

Figure 2. The growth rate of DAW versus different background electron pressure scale length ($\mathbf{L_{pe}}$) from dispersion relation for (a) PFPO-1 and (b) PFPO-2 scenarios. Both cross marks in figures represent the $\mathbf{L_{pe}}$ corresponding to the most unstable locations obtained from linear simulations by the elm-6f module.

Putting the parameters from PFPOs into function (14), figure 2(a)-(b) are obtained to show the growth rate of their respective DAW instability versus electron pressure gradient L_{pe}. The results demonstrate a non-monotonic dependence on the electron pressure characteristic length: as this parameter increases, the DAW is first destabilized and then re-stabilized. This indicates that while L_{pe} serves as a driving term for DAW, the most unstable location for DAW does not necessarily coincide with the position of the minimum characteristic length of electron pressure. Instead, as cross marks signed in both figures, the L_{pe} corresponding to the most unstable DAW mode structure, should be located near the L_{pe} associated with the peak growth rate in the dispersion relation diagram. The flux-limited parallel thermal conduction is also implemented.

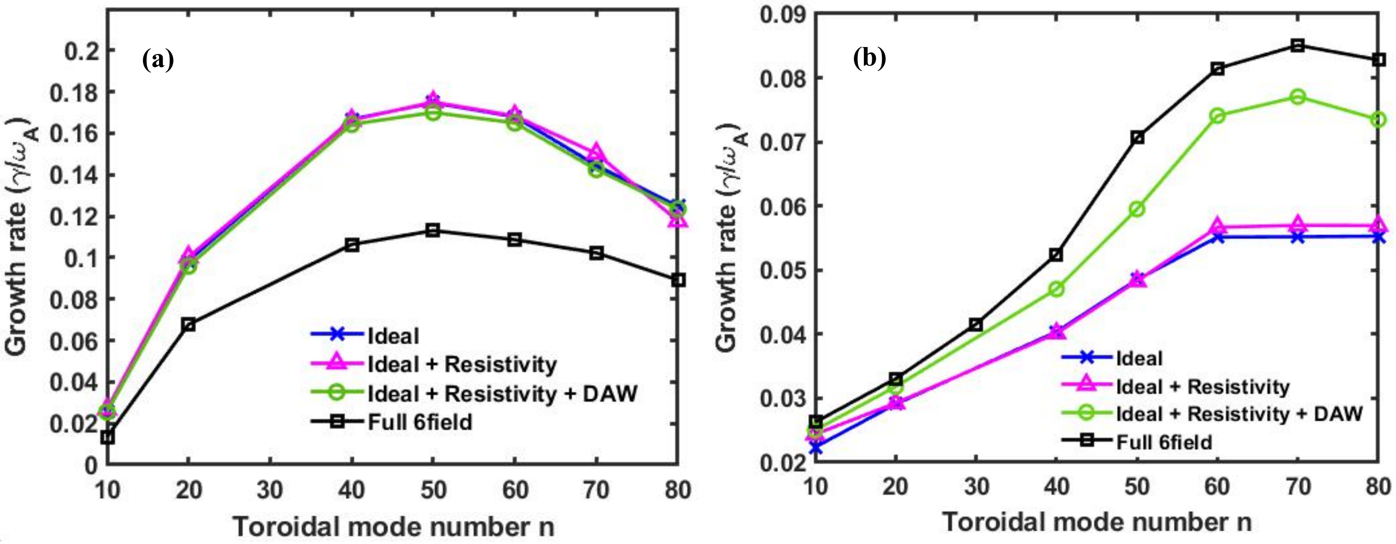

Figure 3. Linear growth rate with different reduced modules of: (a) ITER 5MA PFPO-1 scenario; (b) ITER 7.5MA PFPO-2 scenario.

3.2 Linear analysis

Linear analysis, obtained using BOUT++ turbulence modeling with different physics effects, as illustrated in figure 3, consistently reveals the trigger mechanism and characteristics of the equilibrium. For efficiency, only one-fifth of the torus is simulated. The toroidal mode number of perturbations in the simulations is kept up to 80, which nearly covers the peak linear growth rate. In each plot of figure 3, the blue star curve represents the linear growth rate of the ideal peeling-ballooning mode (PB). When the Spitzer resistivity is considered, the linear growth rate depicted by the magenta triangle curve almost overlaps that of the ideal PB mode. The green curve with circles stands for the growth rate, which further incorporates the DAW, and the black square curve for the linear growth rate with the full six-field non-ideal physical effects. The comparison of these curves reveals that the equilibrium of PFPO-1 in figure 3(a) is primarily destabilized by the ideal ballooning, while the equilibrium of PFPO-2 in figure 3(b) is destabilized by both ideal PB and DAW instability. It should be noted that with the global effects the growth rate behavior after PB coupling shown in figure 3 may differ from isolated DAW analysis. As seen in figures 2(a) and 3(a), the relatively weak DAW component becomes indistinguishable in PB-coupled instabilities.

3.3 Characteristics of ELM nonlinear dynamics

The PFPO-2 equilibrium is selected for nonlinear turbulence simulations to investigate the influence of DAW on turbulent transport in this section. The resistivity η is considered as Spitzer–Härm form, and hyper-resistivity is taken as a constant value $\eta_{\mathrm{H}} = 10^{-16}$ in generalized Ohm's law in Eq. (6) for current diffusion. The

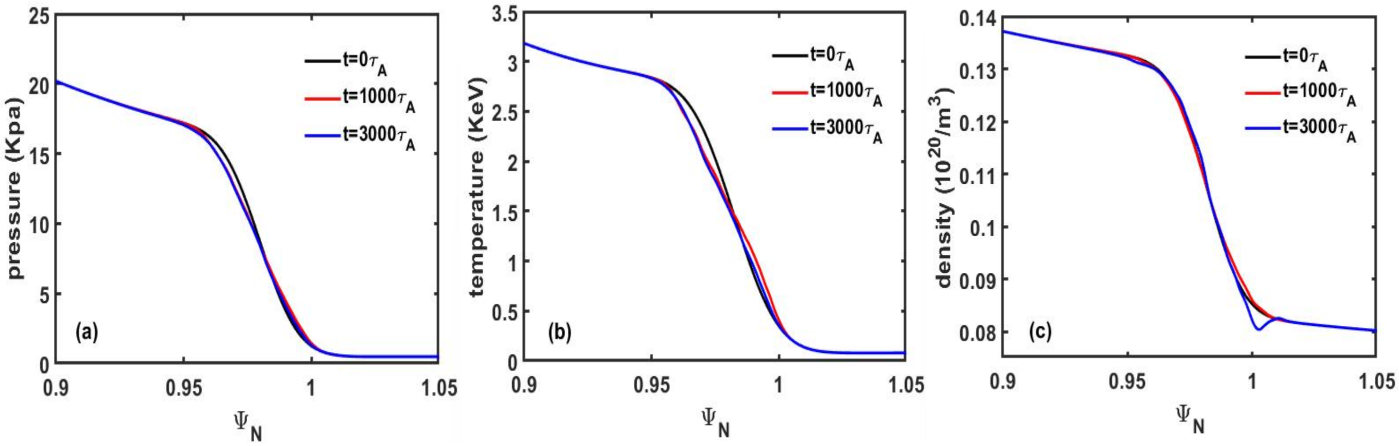

sheath boundary conditions are applied for parallel velocity, parallel sheath current and parallel ion and electron heat fluxes.

Figure 4. The simulated crash at OMP during the ELM bursts of (a) the pressure profile, (b) the electron temperature profile, and (c) the ion temperature profile.

The time evolution of pressure, temperature and density profiles at the outer mid-plane (OMP) during the ELM crash are shown in figure 4. In figure 4(a)-(c), the black curves represent the initial profiles at the start of the simulation, while the red and blue curves depict the profiles at $\mathrm{t}=1000\tau_\mathrm{A}$ and $\mathrm{t}=3000\tau_\mathrm{A}$ of the simulation, respectively. As shown in figure 4(a), the pressure profile gradually collapses inward, and energy is transported outward from the core during $\mathrm{t}=0-1000\tau_\mathrm{A}$, while the pressure profile during $\mathrm{t}=1000-3000\tau_\mathrm{A}$ is not changed too much since the simulation reaches the saturation state. Figure 4(b)-(c) show that the crash range extends to the inner boundary, and the perturbation of temperature contributes more share to the pressure crash. The energy loss ratio from the pressure channel during an ELM burst can be quantified by ELM size and is defined as follow[50,56]:

$$\Delta_{ELM(t)} = \frac{\Delta W_{ped}}{W_{ped}} = \frac{\int_{\mathrm{R_{in}}}^{\mathrm{R_{out}}} dR \oint d\theta \langle P(t)-P_0\rangle_\xi}{\int_{\mathrm{R_{in}}}^{\mathrm{R_{out}}} dR \oint d\theta P_0} \qquad (15)$$

Where ΔW_{ped} is the energy loss and W_{ped} denotes the pedestal stored energy. The symbol $\langle\,\rangle$ means the average over bi-normal periodic coordinate. The lower and upper integral limit $\mathrm{R_{in}/R_{out}}$ refer to the inner radial boundary of the simulation and the peak pressure gradient location, respectively. According to the time evolution of the pressure profile shown in figure 4(a), the calculated ELM size is about 0.5%, indicating a very small ELM.

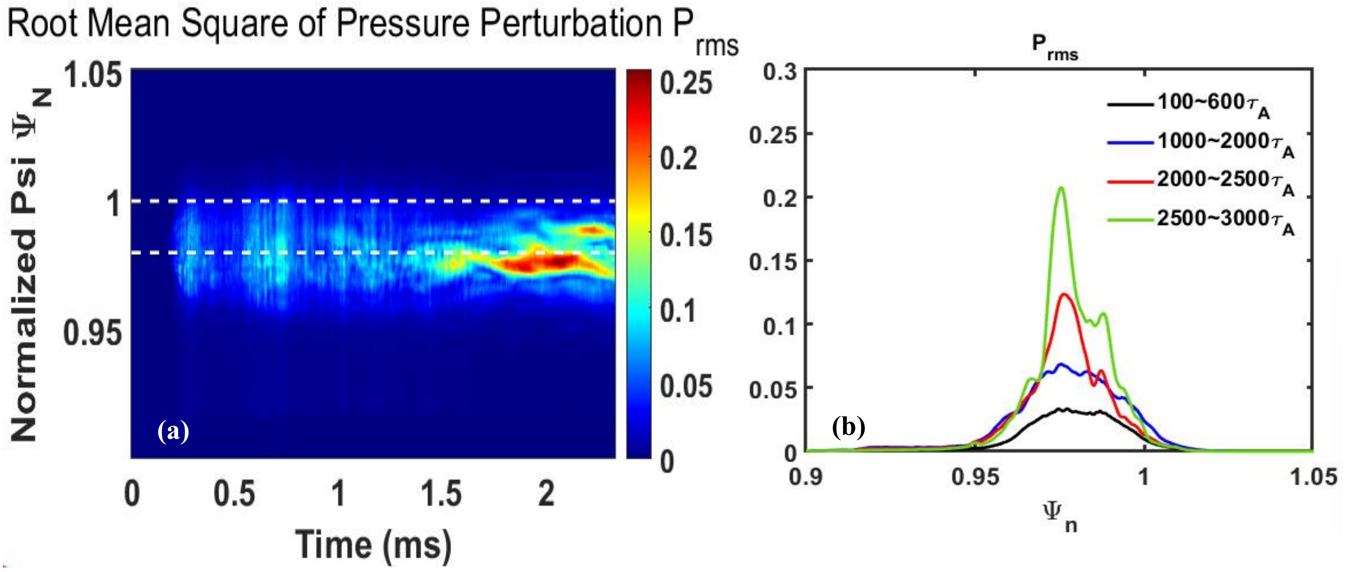

Figure 5. (a) The evolution of P_{rms} at outer mid-plane with time and radial position. The upper white dashed line indicates the position of the separatrix, the white dashed line below represents the position of the peak gradient of pressure. (b) Average radial mode structures of pressure fluctuation at OMP during different periods with τ_A=0.69μs.

Figure 5(a) shows the contour map of the root mean square of the pressure perturbation at OMP as a function of time and radial position. The upper white dashed line marks the position of the separatrix, the region above the separatrix corresponds to the scrape-off layer (SOL), and the white dashed line below indicates the location of the peak pressure gradient. As shown in this figure, the pressure perturbation starts to arise from the position near the peak pressure gradient, then spreads radially to both sides in a bit. The figure illustrates that turbulence in the SOL is generated in the pedestal region and propagates through the separatrix, rather than produced by local perturbations. Since the pressure perturbation is near the boundary of plasma instability, as shown in figure 4(a), the slight evolution of the pressure profile doesn't generate strong turbulence, nor does the turbulence propagate into the SOL. The average radial mode structures of pressure fluctuation at OMP during different periods are displayed in figure 5(b). As indicated by the black and blue curves in figure 5(b), the mode grows at the position of the peak pressure gradient during the linear and early nonlinear stages. In the later nonlinear phases, the mode structure profiles, represented by red and green curves, spread radially to both sides a little, reflecting the slight pedestal collapse due to the small ELM burst.

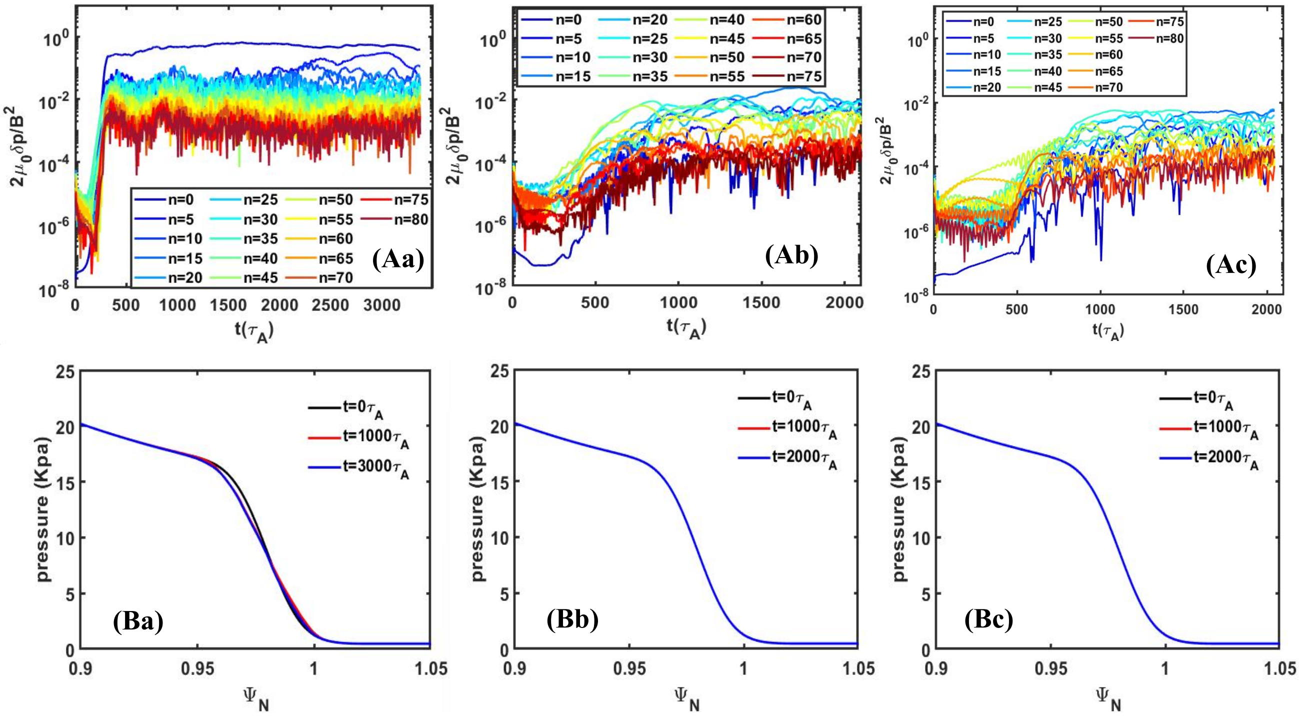

Figure 6. (A) Time evolution of pressure fluctuation for different toroidal mode numbers and (B) the radial pressure profiles at different times. The three columns are for three different linear instability drives: (Aa) and (Ba) with both PB and DAW drives; (Ab) and (Bb) with DAW drive only without PB drive; (Ac) and (Bc) with PB drive only without DAW drive.

3.4 Impact of PB mode and DAW on ELM and turbulence dynamics

Three nonlinear simulations are performed with both PB mode and DAW driving terms, and also for the cases with either one of them in the model to analyse the impact of PB and DAW instabilities on the ELM dynamics. In figure 6, plots in column ‘a’ are the simulation results with both PB and DAW driving; Plots in column ‘b’ are the simulation results without DAW instability driving terms, and plots in column ‘c’ are the simulation results without PB instability driving. Using the Fourier transform, the time evolutions of pressure perturbation at the peak gradient region at the OMP with different toroidal mode numbers during the nonlinear simulations for three cases are shown in the upper row of figure 6. The time evolutions of pressure profiles at the OMP during the ELM crash are shown in the lower row of figure 6, corresponding to the three cases. Figure 4(a) and figure 6(Ba) share the same plot. For the case ‘a’, the linear growth rate is large, leading to a rapid transition to the nonlinear stage. Throughout nearly the whole nonlinear phase, a visible n=0 perturbation (represented by the blue curve) is observed. This indicates that more free energy is redistributed to the zonal component, resulting in the increased energy loss. According to the results for case ‘b’, the linear growth rates decrease obviously after excluding the PB instability driving term. The time period before the nonlinear stage is prolonged, the zonal perturbation disappears, and the amplitude of the disturbance is reduced by nearly one order of magnitude. There is no ELM burst and the pressure profile remains unchanged. By comparing the results of cases 'a' and 'b', we can conclude that the PB instability driving is a necessary condition for pedestal collapse.

This finding is consistent with the well-established theory that PB modes trigger magnetic reconnection, which subsequently leads to the collapse of the pedestal[57,58]. The results in column 'c' of figure 6, which exclude the DAW driving term, are similar to those of case 'b'. The linear growth rates are decreased significantly and the zonal perturbation vanishes. The enhanced interactions between perturbations with different toroidal modes lead to energy dispersion and an overall reduction in disturbance amplitude, which decreases by almost one order of magnitude. Since the perturbation does not grow sufficiently to trigger an ELM before entering the nonlinear stage, there is no ELM burst and the pressure profile remains unchanged. By comparing the results in figure 6, we can find that the PB instability driving is a necessary but insufficient condition for ELM dynamics for this PFPO-2 equilibrium, and the DAW driving can strengthen the turbulence effects induced by PB modes to a certain extent.

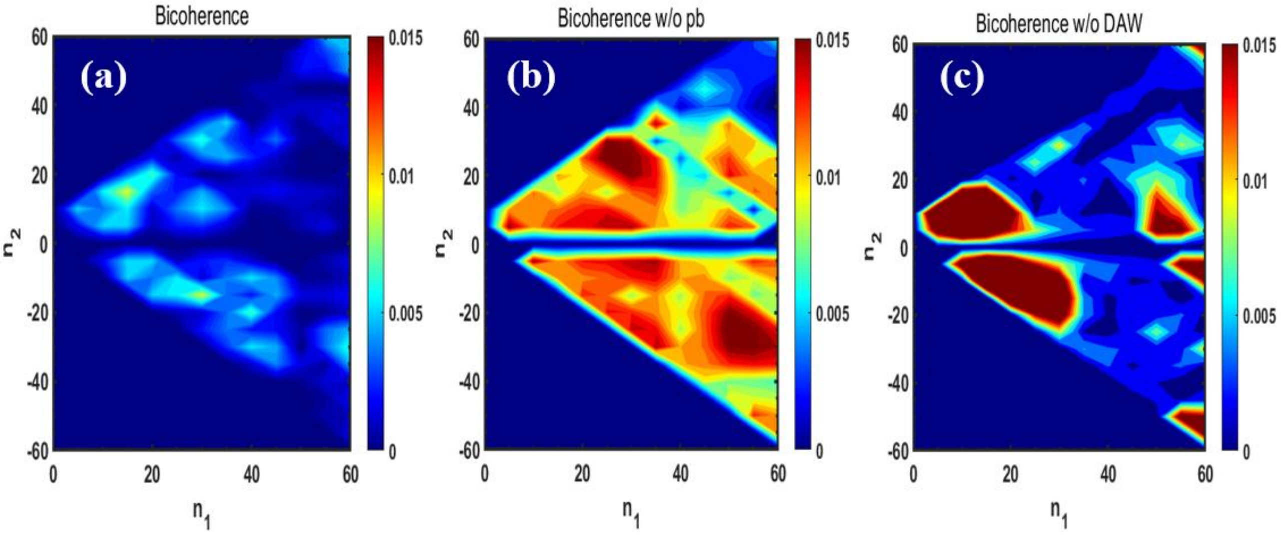

Figure 7. The squared auto-bicoherence $\hat{b}^2_{p_n p_n p_n^{*(n_1,n_2)}}$ of nonlinear PB modes for cases with different linear instability drives: (a) with both PB and DAW drives; (b) with PB drive only without DAW drive; (c) with DAW drive only without PB drive. The (a)-(c) share the same color bar.

Generally, the nonlinear mode coupling intensity has an important effect on the pedestal energy loss. Bi-spectral analysis is a very effective signal processing method to characterize the strength of nonlinear three-wave interactions among fluctuating quantities, and evaluate the degree of correlation between one wave and others[59-62]. The definition is as follows:

$$\widehat{B}(n_1, n_2) = \langle X(n_1)X(n_2)X^*(n_1 + n_2)\rangle \qquad (16)$$

$$\hat{b}^2(n_1, n_2) = \frac{\left|\widehat{B}(n_1, n_2)\right|^2}{\langle |X(n_1)X(n_2)|^2\rangle\langle |X(n_1+n_2)|^2\rangle} \qquad (17)$$

where $\mathrm{X(n)}$ is the space Fourier transform of the fluctuated signal in the toroidal direction, n is the toroidal mode number, and $\mathrm{X^*(n)}$ represents the conjugate of $\mathrm{X(n)}$. In the functions, symbol $\langle\ \rangle$ means perturbation average over different location range and time period. $\widehat{\mathrm{B}}$ is the auto-bicoherence of the pressure fluctuation, and $\hat{\mathrm{b}}^2$ is the squared auto-bicoherence revealing the nonlinear interaction level among the three modes.

The squared auto-bicoherence of pressure fluctuation near the peak gradient region at the OMP during the late nonlinear phase is calculated for the three cases corresponding to figure 6 and are presented in figure 7. In the first plot, the color is lighter; in the second plot, the spectrum is broader; and in the third plot, the spectrum is more concentrated. The darker color in the latter two plots indicates stronger coupling among modes with intermediate and high toroidal mode numbers n. They tend to be ‘multiple-mode’ coupling, which could disperse the free energy triggered by pressure gradient, reduce the energy loss effectively, and decrease the phase coherence time of the fluctuation. By comparing the results in figure 7, it is evident that when

DAW or PB mode driving is not included, the energy loss is little and no ELM burst occurs due to the stronger multiple-mode interaction.

4. Divertor heat flux width

Within BOUT++ framework, turbulence (six-fields two-fluid module) and transport simulation modules are developed separately, utilizing a similar set of Braginskii equations (Transport modules use electrostatic potential instead of the magnetic vector potential) to capture the different physics in different temporal-scales[28-32] . Different modules have different foci: turbulence code mainly focuses on fast turbulence dynamics and scale of up to a few hundred Alfvén times; while the BOUT++ transport module mainly focuses on 2D plasma evolution to steady state on a longer transport time scale. Results of the anomalous thermal diffusivity scan, simulated by BOUT++ transport module in Ref. [23] (section 2.1), reveal two distinct regimes for the heat flux width λ_q: a drift-dominated regime and a turbulence-dominated regime, each exhibiting disparate characteristics. The critical thermal diffusivity χ_c, which identifies two distinct regimes obtained from prior transport simulations[23], is $0.5\mathrm{m}^2/\mathrm{s}$ for PFPO-1 and $0.3\mathrm{m}^2/\mathrm{s}$ for PFPO-2. In this section, we primarily calculate the certain effective electron thermal diffusivity χ_e for the same scenarios (ITER PFPO-1 and PFPO-2) using BOUT++ turbulence module, and combine these results with transport simulations to get which feature regime they lie in. To ensure consistency between the two codes, the simulation grid, geometry and boundary conditions are identical to those used in the transport simulations.

4.1. Prediction of the heat flux width for the PFPO-1

Time evolutions of pressure p profile at the outer mid-plane during the ELM crash are also simulated for the PFPO-1. As shown in figure 8(a), the black curve represents the initial profile at the start of the simulation. The blue curve corresponds to the profile at $t = 2300\tau_A$, which is already a long time to get saturated. The pressure profiles exhibit minimal during the simulation, and the ELM size, obtained by the formula in section 3.1, is approximately 1%.

The definition of radial ion and electron heat flux is given as follow:

$$q_{jr,tur} = \langle \frac{5}{2} n_j T_j \frac{(b_0 \times \nabla\phi)_r}{B_0} \rangle + \langle \kappa_{\parallel,j} \left(\frac{b_0 \times \nabla A_\parallel}{B_0} \right)_r \nabla_\parallel T_j \rangle, \ j = i, e \qquad (18)$$

Where b_0 is the unit vector of the magnetic field and ϕ is electrostatic potential, respectively. The symbol $\langle \, \rangle$ stands for the flux surface average and $\langle f \rangle = 1 \big/ (2\pi)^2 \int_0^{2\pi} d\xi \int_0^{2\pi} f d\theta$ (θ is the poloidal angle, and ξ is the toriodal angle). The flux consists of two components: the first term in the equation represents the convection driven by E × B drift, while the second term corresponds to the conduction induced by the magnetic flutter, with the latter contributing relatively weaker transport effects. (The detailed derivation process of the conductive term is shown in the appendix A.) To facilitate comparison with the previous transport module and other electrostatic numerical codes, we only consider the heat flux induced by E × B turbulence in our simulation, regardless of the heat flux and changes in the magnetic field topology brought by the magnetic perturbation. Of course, PB mode, DAW, and other physical effects still can be taken into account completely. By integrating the heat flux over the separatrix in both poloidal and toroidal directions, we obtain that the heat power

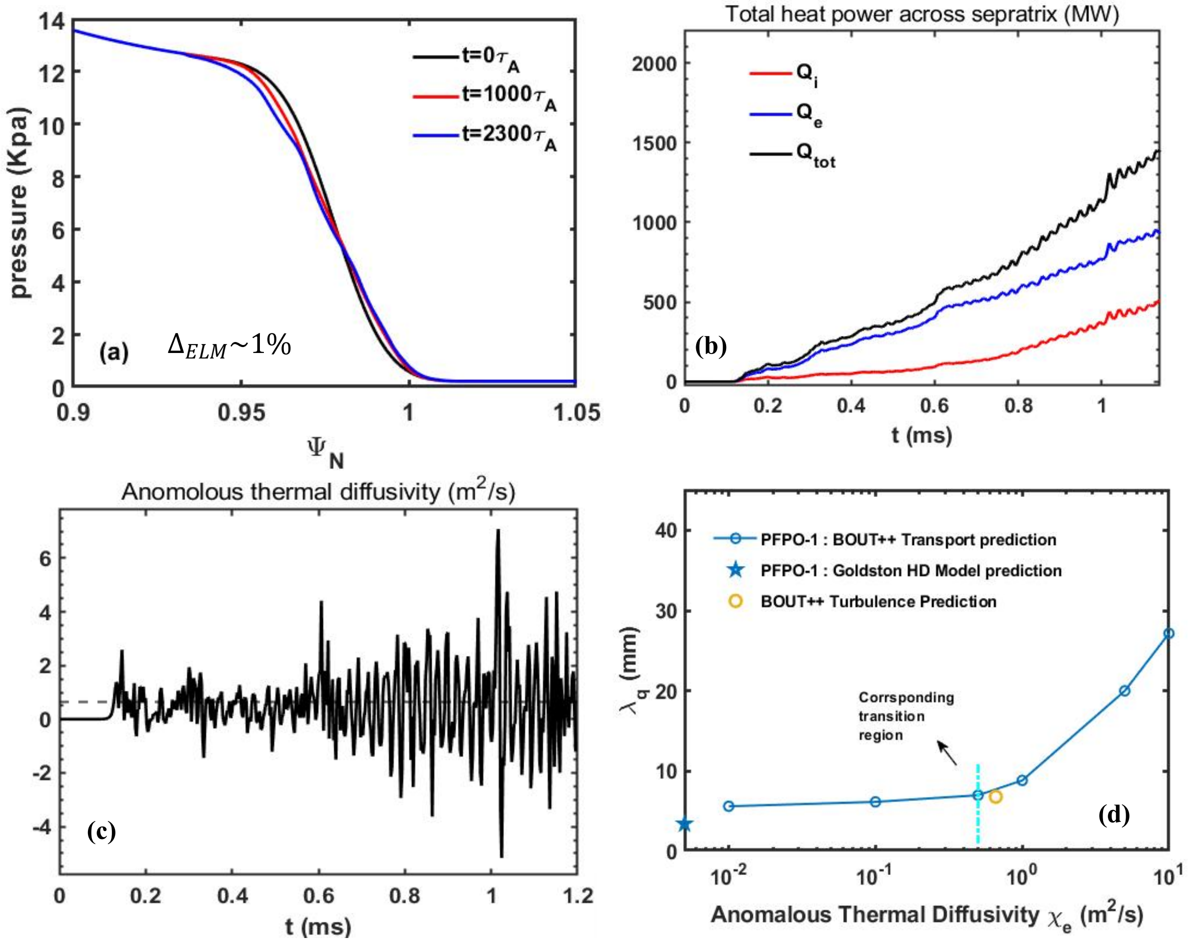

exhibits oscillatory growth over time, and the time integrated heat power is shown in figure 8(b). Averaging the power from the onset of the nonlinear evolution stage to the saturation phase, we get $Q = 3.4$ MW.

Figure 8. Results for PFPO-1: (a) The simulated evolution of pressure profile at the outer mid-plane. (b) $\boldsymbol{E} \times \boldsymbol{B}$ turbulence induced time integrated power across separatrix; (c) Effective electron thermal diffusivity vs simulation time. (d) Comparison between BOUT++ transport and turbulence results of PFPO-2 scenario.

Figure 8(c) presents the equivalent electron thermal diffusivity at the separatrix caused by E × B turbulence, with the time average value $\chi_e = 0.66 \mathrm{m}^2/\mathrm{s}$ during the same period with the power average represented by the dashed line. This value exceeds the critical value $\chi_c = 0.5 \mathrm{m}^2/\mathrm{s}$ obtained by transport simulations, indicating that heat flux width λ_q of the ITER 5MA PFPO-1 scenario should lie near the boundary of two distinct regimes, but closer to the turbulence dominated one. The divertor heat flux width is simulated, and figure 8(d) shows the combination of λ_q from turbulence and transport simulations. The blue circle curve, identical to the curve in figures 2(b) of reference 23, represents the transport simulation results. The orange circle corresponds to effective thermal diffusivity $\chi_\perp$ and heat flux width λ_q from turbulence simulation, which aligns well with the scaling of transport simulation results.

4.2. Prediction of the heat flux width for the PFPO-2

For the ITER 7.5MA PFPO-2 scenario, the heat power across the separatrix calculated by $Q_{sep,j} = \oiint q_{jr,tur}$ over time exhibits oscillatory behavior. It is initially increasing and then decreasing, and the time integrated heat power over time is shown in figure 9(a). The average power from the onset of the nonlinear evolution stage to the saturation phase is $Q = 1.5\ \mathrm{MW}$. The average of the heat power is small. This is probably due to the scenario in the non-activation phase and the small ELM (Δ_{ELM}~0.5%) we got previously. There is no large pedestal crash, so no large amount of thermal energy across the separatrix. According to formula $\chi_e =- \langle\frac{\langle q_{tur}\rangle_{\theta,\zeta}}{\langle n\nabla T\rangle_{\theta,\zeta}}\rangle_t$, we calculate the equivalent electron thermal diffusivity as a function of time in figure 9(b), with the time averaged value of $\chi_e = 0.26\mathrm{m}^2/\mathrm{s}$. The smaller χ_e means that heat flux width λ_q of the ITER 7.5MA PFPO-2 scenario lies within the drift dominant regime. The simulated divertor heat flux widths for ITER 7.5MA PFPO-2 scenario are obtained by Eich-fitting formula[14,23], and the combination of λ_q from turbulence and transport simulations for PFPO-2 is shown in figure 9(c). The orange square curve is identical to the curve shown in figures 2(b) of reference 23. The purple square is the result with corresponding effective thermal diffusivity $\chi_\perp$ and heat flux width λ_q from turbulence simulation, which also follows the scaling of transport simulation results well. The small ELM contributes to the small heat power across the separatrix, as well as the effective thermal diffusivity that is smaller than the critical value χ_c, which results in a relatively narrower heat flux width lying in the drift dominant regime.

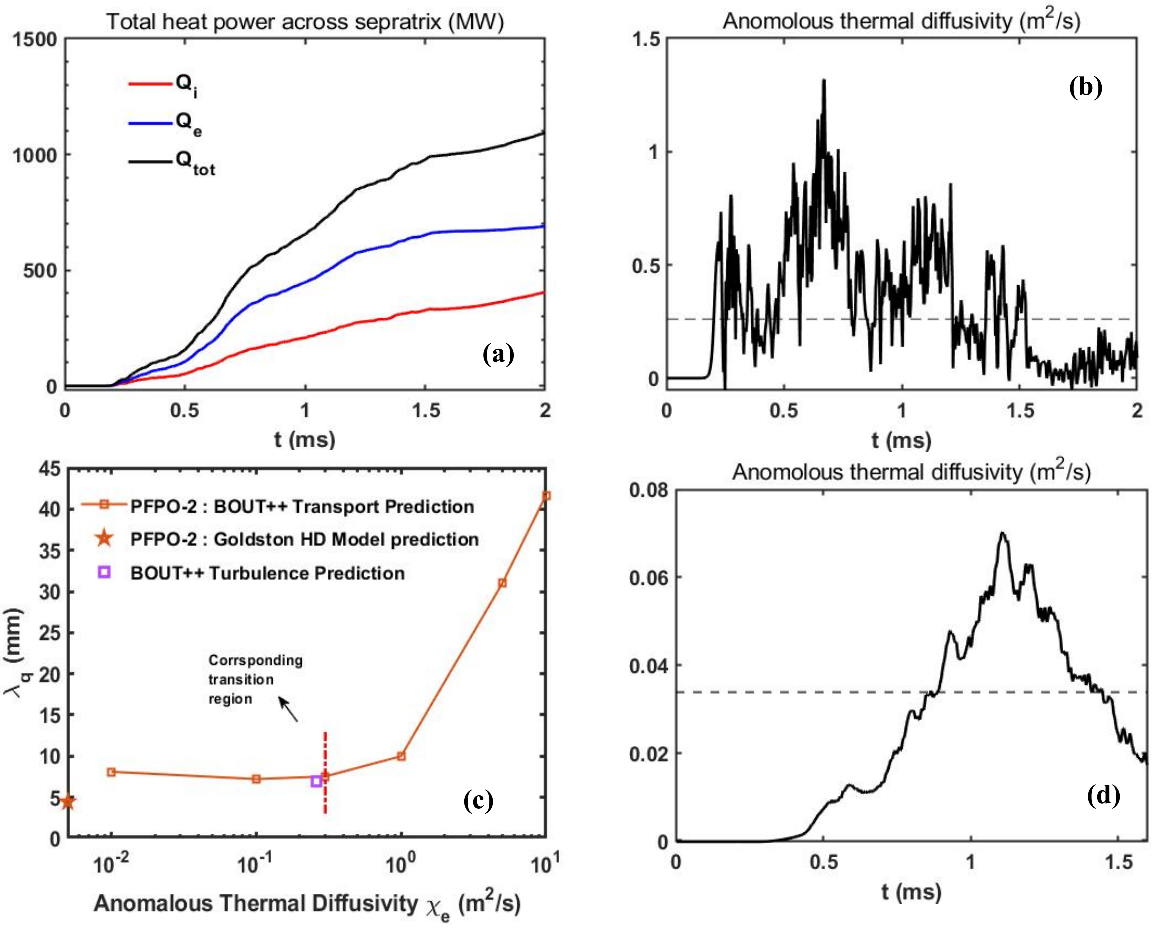

Figure 9. Results for PFPO-2: (a) $\mathbf{E}\times\mathbf{B}$ turbulence induced time integrated power across separatrix; (b) Effective electron thermal diffusivity vs simulation time. (c) Comparison between BOUT++ transport and turbulence results of PFPO-2 scenario. (d) Effective electron thermal diffusivity vs simulation time for the case without DAW mode driving.

To understand the impact of DAW instability driving on the heat flux width, the equivalent electron thermal diffusivity vs time is presented in figure 9(d). The time-averaged value $\chi_e = 0.034\mathrm{m}^2/\mathrm{s}$ during the nonlinear phase is significantly smaller than that obtained with DAW, indicating that the heat flux width lies within the drift-dominated regime. By comparing the results in figure 9(b) and figure 9(d), we can obtain the conclusion that DAW could enhance turbulent transport and thereby increase the effective transport coefficient. If the coefficient increased by DAW driving exceeds the critical value, the heat flux width will transit to be dominated by the turbulent mechanism and so the value will be broadened.

5. Summary

The first and the second PFPO phases with Hydrogen (H) and/or Helium (He) as main ion species in the last ITER Research plan are adopted in this paper to study the impact of DAW driving on the ELM dynamics and the divertor heat flux width. BOUT++ elm-6f turbulence module is employed for both PFPO scenarios with full nonlinear physical mechanisms, as well as comparative analyses of PFPO-2 without PB mode or DAW instability.

Based on the derived dispersion relation from the four-field model with no kinetic effects considered, we give the relationship between the DAW instability and the characteristic length of electron pressure. Results show that the intensity of the DAW instability first enhances and then diminishes as the electron pressure characteristic length increases. Then the linear analysis, obtained using elm-6f module with different physics effects, reveals that the PFPO-1 equilibrium is destabilized by the ideal PB mode, while the PFPO-2 equilibrium is destabilized by the coupling of ideal PB and DAW instability.

Nonlinear simulations of PFPO-2, with both PB mode and DAW instability driving, reveal the presence of a zonal perturbation that causes more perturbative kinetic energy generated and increases outward propagation of pedestal turbulence. The saturated ELM size is 0.5%. When the PB or DAW instability terms are turned off, the zonal perturbation disappears, and the disturbance decreases visibly. In this case, no ELM bursts occur, and the pressure profiles remain unchanged due to the stronger multiple-mode interactions. Nonlinear simulations for PFPO-2 scenario with PB mode and/or DAW instability driving demonstrate that the PB mode is a necessary but not sufficient condition for ELM bursts, and DAW can enhance the turbulence transport triggered by PB mode.

We simulate the SOL turbulence dynamics for the ITER PFPO scenarios and integrate these results with the known outcomes of anomalous thermal diffusivity scans from transport simulations to identify their heat flux width feature and the dominant regime in which they reside. The turbulence-induced average equivalent electron thermal diffusivity of PFPO-1 exceeds the critical value, indicating that the heat flux width of PFPO-1 resides in the turbulence-dominant regime. However, the enlargement is not significant due to the minimal difference between the diffusivity χ_e and its critical threshold χ_c. The average coefficient value of PFPO-2 derived from turbulence simulations is below its critical threshold, indicating that the heat flux width of PFPO-2 is governed by the drift mechanism. The heat flux width obtained from turbulence simulations, with corresponding effective thermal diffusivity for PFPO scenarios, aligns reasonably well with the scaling derived from transport simulation results. These simulations establish a predictive framework for heat flux width and its dominant mechanisms, thereby providing a comprehensive scheme for the prediction of the heat flux width. Furthermore, when the DAW instability is excluded in the nonlinear simulation of the PFPO-2 scenario, the average effective thermal diffusivity decreases by almost an order of magnitude. The comparison indicates that DAW instability driving can increase the transport coefficient by enhancing the turbulent transport, and therefore the heat flux width will be broadened once the transport coefficient exceeds its critical threshold.

Acknowledgment

The authors wish to thank Lynda L. LoDestro and S.H. Kim for providing CORSICA simulation data for the ITER PFPO-1 and PFPO-2 scenarios. This work is supported by the Postdoctoral Fellowship Program of CPSF (Grant No. GZC20232714), the CASHIPS Director ' s Found (Grant Nos. YZJJ2024QN23, YZJJ2024QN26, YZJJ2023QN18), the National Natural Science Foundation of China (Grant Nos. 12505264, 12347176, and 12175275), the National MCF Energy R&D Program of China (Grant No. 2019YFE03030004), the China Postdoctoral Science Foundation (Grant Nos. 2023M733545, 2023M743541), the Anhui Provincial Natural Science Foundation (Grant No. 2408085MA004), and the Science Foundation of ASIPP (Grant No. DSJJ-2023-01). This work is performed under the U.S. Department of Energy by

Lawrence Livermore National Laboratory under Contract No. DE-AC52-07NA27344 and LLNL-JRNL-2015029. This work is also sponsored in part by the Youth Innovation Promotion Association Chinese Academy of Sciences (Y2021114), the Strategic Priority Research Program of Chinese Academy of Sciences under Grant No. XDB0790102, and the Collaborative Innovation Program of Hefei Science Center, CAS, 2021HSC-CIP018. Numerical computations were performed on Hefei advanced computing center, the ShenMa High Performance Computing Cluster in Institute of Plasma Physics.

Appendix A.

In our 6-field model, a reduced two-fluid turbulence simulation model, physics in the parallel and perpendicular direction are separated. As a result, the divergence of the heat flux which affects the perturbed temperature evolution are separated into two parts,

$$\nabla_{\parallel} q_{j\parallel} + \nabla_{\perp} q_{j\perp},$$

And also the heat flux in parallel and perpendicular directions are,

$$q_{j\parallel} =- \kappa_{\parallel j} \nabla_{\parallel} T_j,\ q_{j\perp} =- \kappa_{\perp j} \nabla_{\perp} T_j$$

The symbol $\nabla_{\parallel} = \boldsymbol{b} \cdot \nabla = \left(\boldsymbol{b}_0 - \boldsymbol{b}_0 \times \nabla A_{\parallel}/B_0\right) \cdot \nabla$, which indicates that the parallel gradient operator is not only operates on the equilibrium magnetic field direction but also on the magnetic flutter direction.

Since $\kappa_{\perp j} \ll \kappa_{\parallel j}$, we may ignore the contribution of $q_{j\perp}$ when we calculate the thermal transport and concern the contribution by $q_{j\parallel}$. The parallel heat flux is shown as follow:

$$\boldsymbol{q}_{j\parallel} = (\boldsymbol{b}\boldsymbol{b}) \cdot \boldsymbol{q}_j = \boldsymbol{b} q_{j\parallel},\ \boldsymbol{b} = \boldsymbol{b}_0 - \boldsymbol{b}_0 \times \nabla A_\parallel / B_0 = \boldsymbol{b}_0 + \widetilde{\boldsymbol{b}},$$

If the magnetic perturbations are induced, $A_\parallel \neq 0$, $\boldsymbol{q}_{j\parallel}$ will have the component that points to the cross magnetic flux surface direction. Approximately, the heat flux has a radial component $\widetilde{\boldsymbol{b}} q_{j\parallel}$ that contributes on the radial thermal transport. It is defined as

$$\boldsymbol{Q_j} = \widetilde{\boldsymbol{b}} q_{j\parallel} =- \left(- \boldsymbol{b}_0 \times \nabla A_\parallel / B_0\right) \kappa_{\parallel j} \nabla_\parallel T_j$$

Therefore, the "radial" component is,

$$Q_{jr} \ = \boldsymbol{Q_j} \cdot \boldsymbol{e_r} = \kappa_{\parallel j} \frac{\boldsymbol{e_r} \cdot \boldsymbol{b}_0 \times \nabla A_\parallel}{B_0} \boldsymbol{b} \cdot \nabla T_j$$

After surface averaging, the radial component of thermal transport due to magnetic flutter can be expressed as:

$$< Q_{jr} > = \ < \kappa_{\parallel j} \left(\frac{\boldsymbol{b}_0 \times \nabla A_\parallel}{B_0} \right)_r \nabla_\parallel T_j >$$

References:

[1]. Wagner F et al 1982 Phys. Rev. Lett. 49 1408

[2]. Hawryluk R.J. et al 2009 Nucl. Fusion 49 065012

[3]. Leonard A.W. 2014 phys. Plasmas 21 090501

[4]. Zohm H. et al 1996 Plasma Phys. Controlled Fusion 38 105

[5]. Connor J.W. et al 1998 Plasma Phys. Controlled Fusion 40 531

[6]. Loarte A. et al 2007 Nucl. Fusion 47 S203

[7]. K. T. Tsang et al 1978 PRL

[8]. P. Manz et al 2020 Nucl. Fusion 60 096011

[9]. Z.X. Liu et al 2022 Nucl. Fusion 62 086029

[10]. Liu Z.X. et al 2016 Phys. Plasmas 23 120703

[11]. Yong Lang et al 2022 Nucl. Fusion 62 086018

[12]. Nami Li et al 2022 Nucl. Fusion 62 096030

[13]. Eich T. et al 2011 Phys. Rev. Lett. 107 215001

[14]. Eich T. et al 2013 Nucl. Fusion 53 093031

[15]. Kukushkin A. et al 2013 J. Nucl. Mater. 438 S203

[16]. Goldston R.J. 2012 Nucl. Fusion 52 013009

[17]. Chang C.S. et al 2017 Nucl. Fusion 57 116023

[18]. Myra J.R. 2015 Phys. Plasmas 22 042516

[19]. Li Z.Y. et al 2019 Nucl. Fusion 59 046014

[20]. Kaveeva E. et al 2020 Nucl. Fusion 60 046019

[21]. Xu X.Q. et al 2019 Nucl. Fusion 59 126039

[22]. Li N.M. et al 2020 AIP Advances 10 015222

[23]. He X.X et al 2022 Nucl. Fusion 62 056003

[24]. ITER Organization 2018 Technical Reports ITR-18-003

[25]. Schneider M. et al 2019 Nucl. Fusion 59 126014

[26]. Kim S.H. et al 2017 Nucl. Fusion 57 086021

[27]. Dudson B D et al 2009 Commun. Comput. Phys. 180 1467

[28]. Xia T Y et al 2013 Nucl. Fusion 53 073009

[29]. Xia T Y et al 2015 Nucl. Fusion 55 113030

[30]. Wang Z.H. et al 2014 Nucl. Fusion 54 043019

[31]. Li N.M. et al 2018 Comput. Phys. Commun. 228 69–82

[32]. Zhu B. et al 2021 Comput. Phys. Commun. 267 108079

[33]. Xia T Y et al 2017 Nucl. Fusion 57 116016

[34]. Deng G.Z. et al 2020 Nucl. Fusion in press

[35]. Lin. X. et al 2025 Phys. Plasmas 32, 012503

[36]. Li N.M. et al 2024 J. Plasma Phys. 90 5900117

[37]. Li Y.L. et al 2025 Nucl. Fusion 65 026027

[38]. Li N.M. et al 2022 Nucl. Fusion 62 096030

[39]. Li N.M. et al 2023 Nucl. Fusion 63 124005

[40]. Y.L. Li et al 2022 Nucl. Fusion 62 066018

[41]. Xu X.Q. et al 2025 Nuclear Materials and Energy 42 101866

[42]. Chen B. et al 2017 Nucl. Fusion 57 116025

[43]. Chen B. et al 2018 Phys. Plasmas 25 055905

[44]. Li N.M. et al 2020 AIP Advances 10 015222

[45]. Tang T.F. et al 2018 Plasma Phys. Control. Fusion submitted

[46]. Li Z.Y. et al 2024 Communications physics 7:96

[47]. Li Z.Y. et al 2018 Nucl. Fusion 58 016018

[48]. Tang T.F. et al 2022 Nucl. Fusion 62 016008

[49]. Y. B. Wu et al 2018 Plasma Phys. Control. Fusion 60, 055007

[50]. He X.X. et al. 2021 AIP Advances 11 035334

[51]. Y.R. Zhu et al 2020 Nucl. Fusion 60 046014

[52]. Kim S.H. et al 2016 Nucl. Fusion 56 126002

[53]. Kim S.H. et al 2018 Nucl. Fusion 58 056013

[54]. Huang Y.Q. 2020 [Doctoral dissertation, University of Science and Technology of China]

[55]. Ma J.F. 2015 [Doctoral dissertation, The University of Texas at Austin]

[56]. Xi P.W. et al 2013 Nucl. Fusion 53 113020

[57]. P.B. Snyder, et al., Phys. of Plasmas, 9 (5), 2002, p. 2037

[58]. Xu et al 2010 Physical Review Letters, Vol. 105, 175005

[59]. Holland C. et al 2002 Plasma Physics and Controlled Fusion 44 (5A): A453-A457

[60]. Kim Y. C. et al 1978 Physics of Fluids 21 (8): 1452.

[61]. Kim Young et al 1979 IEEE Trans. Plasma Sci. PS-7, 120-131

[62]. Lan T. et al 2008 Plasma Physics and Controlled Fusion 50 (4): 045002